


Random alloy thick AlGaAsSb avalanche photodiodes on InP substrates ^{EP}

Cite as: Appl. Phys. Lett. **120**, 071101 (2022); <https://doi.org/10.1063/5.0067408>

Submitted: 16 August 2021 • Accepted: 31 January 2022 • Published Online: 14 February 2022

 S. Lee, B. Guo, S. H. Kodati, et al.

COLLECTIONS

 This paper was selected as an Editor's Pick



View Online



Export Citation



CrossMark

ARTICLES YOU MAY BE INTERESTED IN

[Spectral modulation of blocked-impurity-band hybrid structure terahertz detector](#)
Applied Physics Letters **120**, 071102 (2022); <https://doi.org/10.1063/5.0082048>

[2.7 \$\mu\text{m}\$ quantum cascade detector: Above band gap energy intersubband detection](#)
Applied Physics Letters **120**, 071104 (2022); <https://doi.org/10.1063/5.0076856>

[Voltage control of magnetism with magneto-ionic approaches: Beyond voltage-driven oxygen ion migration](#)

Applied Physics Letters **120**, 070501 (2022); <https://doi.org/10.1063/5.0079762>

 QBLOX



1 qubit

Shorten Setup Time

Auto-Calibration
More Qubits

Fully-integrated

Quantum Control Stacks
Ultrastable DC to 18.5 GHz
Synchronized <<1 ns
Ultralow noise



100s qubits

[visit our website >](#)

Random alloy thick AlGaAsSb avalanche photodiodes on InP substrates

Cite as: Appl. Phys. Lett. **120**, 071101 (2022); doi: [10.1063/5.0067408](https://doi.org/10.1063/5.0067408)

Submitted: 16 August 2021 · Accepted: 31 January 2022 ·

Published Online: 14 February 2022







View Online



Export Citation



CrossMark

S. Lee,¹  B. Guo,² S. H. Kodati,¹ H. Jung,¹ M. Schwartz,¹ A. H. Jones,² M. Winslow,³ C. H. Grein,³ T. J. Ronningen,¹ 
J. C. Campbell,²  and S. Krishna^{1,a)} 

AFFILIATIONS

¹Department of Electrical and Computer Engineering, The Ohio State University, Columbus, Ohio 43210, USA

²Department of Electrical and Computer Engineering, University of Virginia, Charlottesville, Virginia 22904, USA

³Department of Physics, University of Illinois, Chicago, Illinois 60607, USA

^{a)} Author to whom correspondence should be addressed: krishna.53@osu.edu

ABSTRACT

We demonstrate low noise random alloy (RA) $\text{Al}_{0.85}\text{Ga}_{0.15}\text{AsSb}$ (hereafter AlGaAsSb) avalanche photodiodes (APDs) nearly lattice-matched to InP substrates. In contrast to digital alloy (DA), RAs are manufacturable due to the ease of growth. The 910 nm-thick RA AlGaAsSb was grown at a low temperature around 450 °C to mitigate phase separation by suppressing surface mobility of adatoms. The high quality of the RA AlGaAsSb material was verified by x-ray diffraction, Nomarski, and atomic force microscope images. Capacitance–voltage measurement found that the background doping concentration was $6\text{--}7 \times 10^{14} \text{ cm}^{-3}$, indicating very low impurity density in the RA AlGaAsSb material. Current–voltage measurements were carried out under dark condition and 455 nm laser illumination at room temperature. The breakdown occurs at -58 V . The dark current density at a gain of 10 was found to be $70 \mu\text{A}/\text{cm}^2$. This value is three orders of magnitude lower than previously reported DA $\text{AlAs}_{0.56}\text{Sb}_{0.44}$ APDs [Yi *et al.*, Nat. Photonics **13**, 683 (2019)], one order of magnitude lower than DA AlGaAsSb [Lee *et al.*, Appl. Phys. Lett. **118**, 081106 (2021)], and comparable to RA AlInAsSb APDs [Kodati *et al.*, Appl. Phys. Lett. **118**, 091101 (2021)]. In addition, the measured excess noise shows a low k (the ratio of impact ionization coefficients) of 0.01. These noise characteristics make the RA AlGaAsSb multiplier suitable for commercial applications, such as optical communication and LiDAR systems.

Published under an exclusive license by AIP Publishing. <https://doi.org/10.1063/5.0067408>

Avalanche photodiodes (APDs) are one of the crucial components in a wide range of short-wavelength infrared (SWIR, 1.55 and $2 \mu\text{m}$) applications, such as optical communication¹ and LiDAR.² Unlike conventional pin photodiodes, APDs have internal gain (M) that amplifies a weak input signal and can provide an improved signal-to-noise ratio. However, avalanche multiplication gain also results in excess noise originating from gain fluctuation due to the stochastic process of impact ionization events. The excess noise of an APD can be characterized by its excess noise factor [$F(M)$] that is given by McIntyre's local field theory,³

$$F(M) = kM + (1 - k) \left(2 - \frac{1}{M} \right). \quad (1)$$

Here, k is the ratio between the electron (α) and hole (β) impact ionization coefficients and is less than 1 for electron-APDs ($k = \beta/\alpha$). Based on Eq. (1), it is essential to lower the k value to minimize the $F(M)$ of an APD. Reducing k is possible by selecting materials that present favorable α and β .

Commercially available SWIR APDs utilize the separate absorption, charge, and multiplication (SACM) structure. In a SACM design, the heterostructure is designed such that the high electric field is present in the multiplication region (wide bandgap material) to achieve high gain, while the absorber (narrow bandgap material) is situated in the low electric field region to mitigate tunneling dark current. This structure enables one to optimally design the properties of the absorber and multiplier separately, thereby improving the device performance. Most commercial SACM APDs on InP substrates employ an InGaAs absorber (1.55 μm wavelength absorption). The multiplication regions are based on InP⁴ or AlInAs⁵ lattice-matched to InP substrates. However, the performance of such APDs is limited by their large k values (k of InP and AlInAs are ~ 0.5 ⁶ and ~ 0.2 ,⁷ respectively). To reduce k further, some researchers have used a thin multiplication layer ($< 200 \text{ nm}$), which can take advantage of the dead space.⁸ As a result, the probability density function of the impact ionization event becomes contracted (more deterministic), resulting in lower excess noise.^{9,10} On the other hand, other researchers have recently reported

that a thick multiplication layer (>1000 nm) can also achieve an extremely low excess noise.^{11,12} Several ternary and quaternary alloys on InP substrates have been explored as thick multipliers to reduce the k further.^{11–14} However, since most ternary and quaternary alloys on InP substrates have been known to experience phase separation during random alloy (RA) growth,^{15,16} growing high-quality thick material is a significant challenge. For thick materials to be effective, the defect density is a critical consideration since increased defect density due to effects, such as phase separation, can limit the performance of the APDs. The digital alloy (DA) growth technique has recently overcome this growth challenge and assisted in growing several materials on InP substrates using two alternating layers that do not undergo phase separation.^{12,13} As a result, thick $\text{Al}_x\text{Ga}_{1-x}\text{As}_y\text{Sb}_{1-y}$ on InP substrates, including $\text{AlAs}_{0.56}\text{Sb}_{0.44}$ (<1550 nm)¹² and $\text{Al}_{0.85}\text{Ga}_{0.15}\text{As}_{0.56}\text{Sb}_{0.44}$ (~ 1000 nm),¹³ have been grown using the DA technique by molecular beam epitaxy (MBE), and low values of k (0.005–0.01) have been demonstrated. However, DA is challenging to grow for the mixed As/Sb alloys due to a large number of mechanical shuttering operations. In DA growth of As/Sb mixed alloys, there is anion exchange at interfaces for short shuttering times.^{17,18} Since the As atom has stronger bonding strength to group III atoms than the Sb atom, residual As atoms from the previous As-containing layer can diffuse into the Sb-containing layer at the interfaces, leading to rough interfaces.^{19–21} Thus, excessive As/Sb shuttering can give rise to many imperfect interfaces (impurities), which significantly affects material quality and carrier transport. A large number of shutter operations can also cause a buildup of Sb on the back of the shutter during DA growth. These Sb flakes can force the suspension of a growth campaign and lead to long downtime for MBE chamber maintenance. On the other hand, RA growth in which the temperature of the effusion cells controls the composition of the layers has practical advantages over DA growth since it does not suffer from the deleterious effects described above. Moreover, RA is more suited for commercialization since the crystal can also be grown by metal-organic chemical vapor deposition (MOCVD), the primary workhorse tool for the optoelectronic semiconductor manufacturing industry. One way to reduce the phase separation in RA is to use low

growth temperatures. Low growth temperature suppresses mobility of the adatoms, preventing the alloy from being immiscible.²² Tomasulo *et al.* have demonstrated that high-quality $\text{Al}_{1-x}\text{In}_x\text{As}_{1-y}\text{Sb}_y$ can be grown on InP substrates at <405 °C, with RMS surface roughness of ~ 3 Å.²² Kodati *et al.* demonstrated a RA $\text{Al}_{0.79}\text{In}_{0.21}\text{As}_{0.74}\text{Sb}_{0.26}$ (AlInAsSb) APD on InP substrates grown at around 450 °C, and this RA AlInAsSb APDs showed a low k (~ 0.018) and lower dark current ($82 \mu\text{A}/\text{cm}^2$ at a gain of 15)¹⁴ than DA AlAsSb¹² and DA AlGaAsSb APDs.¹³

This paper explores an RA-grown, thick $\text{Al}_{0.85}\text{Ga}_{0.15}\text{As}_{0.56}\text{Sb}_{0.44}$ (AlGaAsSb) multiplier. We have recently reported DA-grown, 1000 nm thick AlGaAsSb APDs with low-noise characteristics and high gain with long-term stability than the AlAsSb APDs.¹³ It is found that the RA AlGaAsSb APDs can have similar performance to their DA while having all benefits from the ease of the material growth. We discuss the material growth, characterization, and APD performance of these RA AlGaAsSb multipliers.

Figure 1(a) illustrates the schematic structure of a p-i-n AlGaAsSb APD. First, the device stacks were grown on epi-ready, 3 in. semi-insulating, on-axis InP substrates. Typically, the alloys on the InP substrate have been grown at 500 °C because it is known to achieve high-quality materials while preventing significant In desorption from occurring at above 520 °C.^{23–26} However, in this paper, the growth temperature of the AlGaAsSb alloy was 450 °C to avoid phase separation. The surface temperature of the substrate was measured by the band edge temperature measurement method. When the growth temperature is high enough in this material system, the Al, Ga, As, and Sb are not miscible, resulting in phase separation. However, when we reduce the growth temperature, the surface adatom mobility is also suppressed so that the growth can be done before the system reaches equilibrium conditions. This avoids phase separation. In this case, growth rate and V/III ratio play important roles in achieving a high quality material. For the p-i-n AlGaAsSb layers, the growth rate was $0.5 \mu\text{m}/\text{h}$, and the V/III flux ratio was ~ 5 . The $\text{n}^{++}\text{-In}_{0.53}\text{Ga}_{0.47}\text{As}$ (InGaAs) buffer layer was grown to initiate the entire growth of the device structure with a smooth surface. This layer also acts as a bottom contact layer, and the thickness was chosen to be 500 nm to achieve a

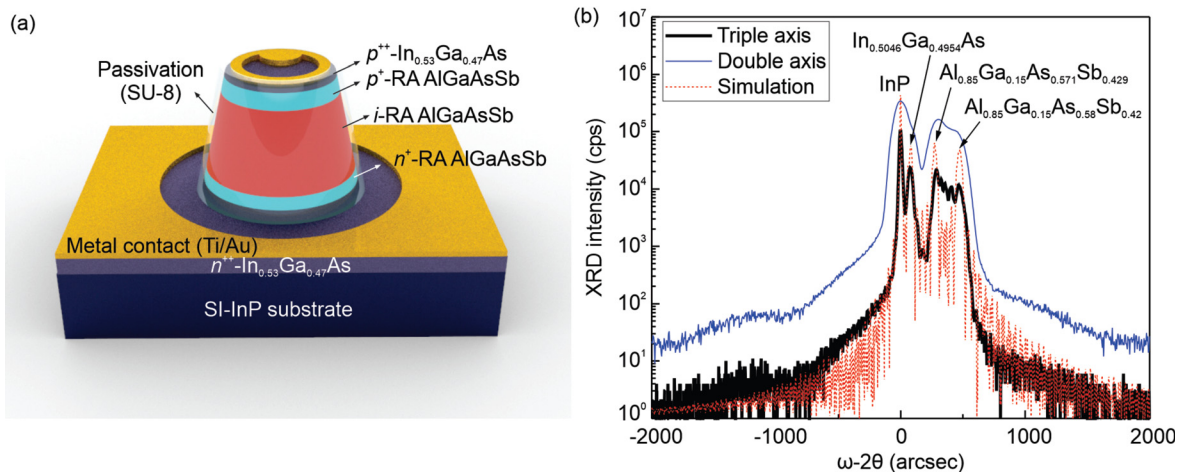


FIG. 1. (a) Schematic device structure and (b) the measured and simulated x-ray diffraction (XRD) of the RA AlGaAsSb APD.

proper wet-etch depth easily. After that, the p^+i (unintentional doping, UID)- n^+ AlGaAsSb structure was grown as RA. Here, the thickness of the UID AlGaAsSb multiplication layer was 910 nm. Before the growth of AlGaAsSb layers, we carried out multiple AlGaAsSb calibration runs to achieve the desired composition. Finally, a 20 nm highly doped p^{++} -InGaAs top contact layer was added as a cap to prevent surface oxidation and ensure low series resistance. For InGaAs top and bottom layers, the growth was performed at 500 °C, and the growth temperature was changed during the growth pause between InGaAs and AlGaAsSb layers. The device fabrication process of p - i - n AlGaAsSb APDs was performed with the conventional lithography and citric acid-based wet-etch method. Ti/Au was used for metal Ohmic contact, and SU-8 was used for surface passivation to cover the sidewalls of the mesa. More details about the fabrication steps can be found elsewhere.^{13,14,26}

Figure 1(b) shows the x-ray diffraction (XRD) result on the RA AlGaAsSb APDs. The blue and black lines indicate the measured XRD curves in the double and triple axes, respectively. It is hard to observe all relevant peaks with double-axis, so a high-resolution triple-axis XRD measurement was performed. Unlike the XRD curve taken in the double-axis, several XRD peaks are resolved in the triple-axis XRD curve. There are two sharp peaks near 0 arcsec corresponding to InP substrate and InGaAs buffer layers. Moreover, there are several peaks in the range from +200 to +400 arcsec, which come from the RA AlGaAsSb alloy. The several AlGaAsSb XRD peaks may originate from a slight change in the As/Sb flux because of a small fluctuation in the surface temperatures when the different epi layers, such as p , i , and n , are being grown. Assuming that the flux of group III (Al and Ga) is constant throughout the growth, and no considerable relaxation presents in between the epi-layers and the substrate, the composition of the AlGaAsSb layer can be, by XRD simulation, estimated to be in a range from $Al_{0.85}Ga_{0.15}As_{0.571}Sb_{0.429}$ to $Al_{0.85}Ga_{0.15}As_{0.58}Sb_{0.42}$, indicating a composition control within about 1%. Additionally, Nomarski and AFM images were taken to examine the surface quality of the RA AlGaAsSb alloy, as shown in Fig. 2. The Nomarski microscopy image [Fig. 2(a)] shows a very smooth surface morphology, and AFM images [Fig. 2(b)] reveal a good root mean square (RMS) roughness of 1.74 Å, indicating that the low adatom mobility helps to improve the material quality of the AlGaAsSb alloy.

Since the RA AlGaAsSb alloy has an indirect bandgap (E_g), the E_g cannot be determined by photoluminescence. This is because the PL intensity is weak. Therefore, to determine the bandgap of the RA AlGaAsSb, a quantum efficiency (QE) measurement was carried out at room temperature (RT), as shown in Fig. 3(a). The measurement was done under -6 V, near a bias point where the device is fully depleted. The Franz-Keldysh effect due to the applied bias is negligible for an indirect gap. The highest QE is about 26.5% at 2.01 eV (615 nm).

For an indirect gap material, QE (\propto responsivity \propto absorption coefficient) can be written as the following expression:²⁷

$$QE \propto (E_{ph} - E_g)^2.$$

Here, E_{ph} is the photon energy. Therefore, the E_g can be accurately determined by linear interpolation near the cutoff tail in the QE spectrum.²⁷ Accordingly, $QE^{1/2}$ was plotted as a function of photon energy, as shown in Fig. 3(b). The x-intercept of the linear fitted line (red dashed line) indicates that the E_g of the RA AlGaAsSb alloy is 1.52 eV. This E_g is similar to the previously reported bandgap of thin RA AlGaAsSb APDs²⁷ and DA AlGaAsSb APDs.¹³

Figure 4(a) shows capacitance–voltage (CV) and depletion width of the RA AlGaAsSb APD for a 200 μ m diameter device at RT. As seen in Fig. 4(a), the capacitance drastically drops and saturates near -4 V. This implies that the device is almost entirely depleted near -4 V. To calculate depletion width and background doping concentration, we used a dielectric constant of 11.41²⁷ and a 910 nm UID layer thickness. This thickness was obtained by secondary ion mass spectroscopy (SIMS), as shown in Fig. 4(b). Figure 4(c) shows the calculated background doping concentration (n_{bg}) as a function of depletion width. The n_{bg} was around $6\text{--}7 \times 10^{14} \text{ cm}^{-3}$, indicating very low impurity density in the AlGaAsSb material. This value is about two orders of magnitude lower than DA AlGaAsSb APDs.¹³ The lower n_{bg} of the RA is likely due to the absence of the interface states. The RA AlGaAsSb does not have any interface states, while the DA does. In some As/Sb superlattices (SLs), such as InAs/AlSb SL^{28,29} or InGaAs/GaAsSb SL,³⁰ interface states were found. Those act as impurities in the materials and, therefore, contribute to the n_{bg} .

The current–voltage (IV) measurement under dark conditions for a 100 μ m diameter device is illustrated in Fig. 5(a). Breakdown (V_{BR}) occurs around -58 V, which corresponds approximately to the critical breakdown field of 580 kV/cm. The V_{BR} of RA is slightly higher

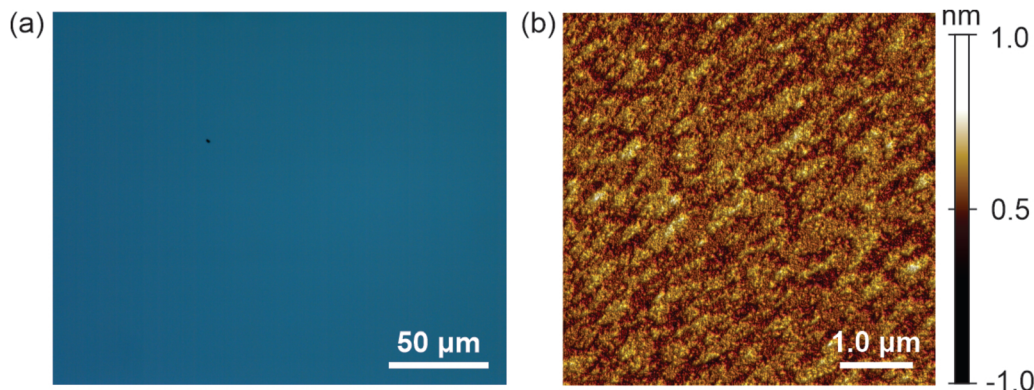


FIG. 2. (a) Nomarski and (b) AFM images of the RA AlGaAsSb APD.

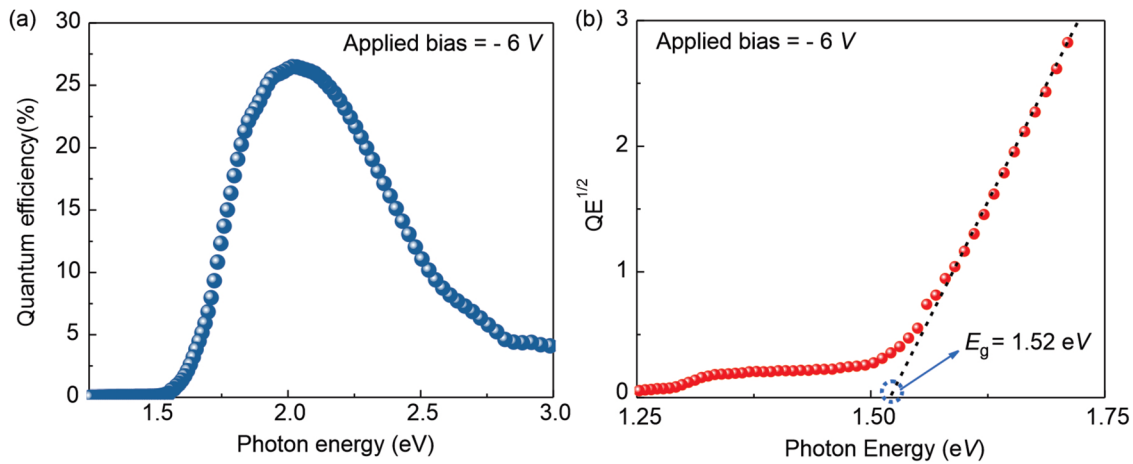


FIG. 3. (a) The measured quantum efficiency (QE) of the RA AlGaAsSb APD and (b) the plot of $QE^{1/2}$ as a function of photon energy to extract the indirect bandgap of the RA AlGaAsSb alloy.

than that of the previously reported DA.¹³ The difference of V_{BR} of RA and DA originates from the discrepancy of the peak electric fields due to the UID background doping difference between RA and DA. The forward bias IV shows that the current sharply increases and hits the 1 mA instrument compliance limit within 1 V, meaning that the contact resistance is sufficiently low.

The dark current, photocurrent, and gain curves of a 150 μm -diameter device are illustrated in Fig. 5(b). The photocurrent was measured with 455 nm laser illumination to ensure a nearly pure electron injection profile. The absorption coefficient of the AlGaAsSb APDs was extracted by ellipsometry measurement, and its appropriate method is described in Ref. 31. The extracted absorption coefficient at 455 nm was $\sim 1.3 \times 10^5 \text{ cm}^{-1}$. According to absorption length calculation based on Beer Lambert's law, 98% of the incident laser intensity was absorbed within the 300 nm $\text{p}^+\text{-AlGaAsSb}$ cladding layer, ensuring that nearly pure electron injection was achieved. The calculated gain gradually increases from -30 to -56 V and peaks at ~ 20 .

To understand the dominant dark current mechanism in the RA AlGaAsSb APDs, variable area diode analysis (VADA) was performed

on the device diameters of 60, 80, 100, and 150 μm . Figure 6 shows the measured dark current of the RA AlGaAsSb APDs as a function of device radius. The dark current scales linearly with the radius. This indicates that the dark current of the RA AlGaAsSb APDs is primarily limited by surface leakage dark current, inferring that an improved surface passivation technique could decrease total dark current further. Regardless of high surface dark current in the RA AlGaAsSb APDs, the total dark current density at a gain of 10 was $\sim 70 \mu\text{A}/\text{cm}^2$. This value is about an order of magnitude lower than the DA AlGaAsSb APDs,¹³ three orders of magnitude lower than the DA AlAsSb,¹² and comparable to the RA AlInAsSb APDs.¹⁴ The RA AlGaAsSb APDs show two times lower dark current than the DA AlGaAsSb APDs ($\sim 145 \mu\text{A}/\text{cm}^2$).³² This is mainly because of the lower peak electric field of the RA AlGaAsSb APDs, which is caused by the lower background doping concentration of the UID layer.

Figure 7 shows the measured $F(M)$ as a function of gain for a 100 μm -diameter device. The measurements were made using an Agilent 8973 noise figure analyzer and 445 nm laser illumination. The k of 0.01 was extracted by using Eq. (1). This value is roughly two

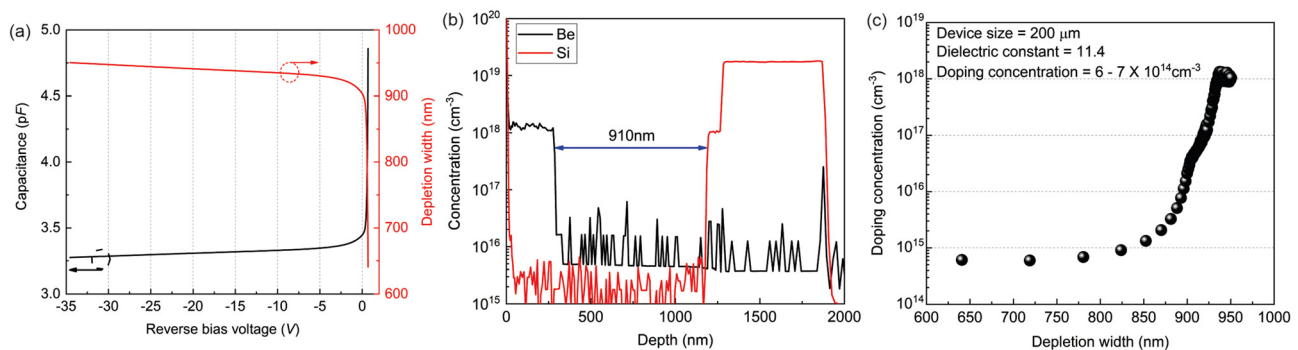


FIG. 4. (a) The result of the CV measurement on the RA AlGaAsSb APD. The black and red solid lines indicate capacitance and the calculated depletion width, respectively. (b) The result of the SIMS measurement on the RA AlGaAsSb APD. The doping profile of Si and Be dopants helps to accurately determine the thickness of the UID layer and estimate (c) the background doping concentration of the RA AlGaAsSb APD.

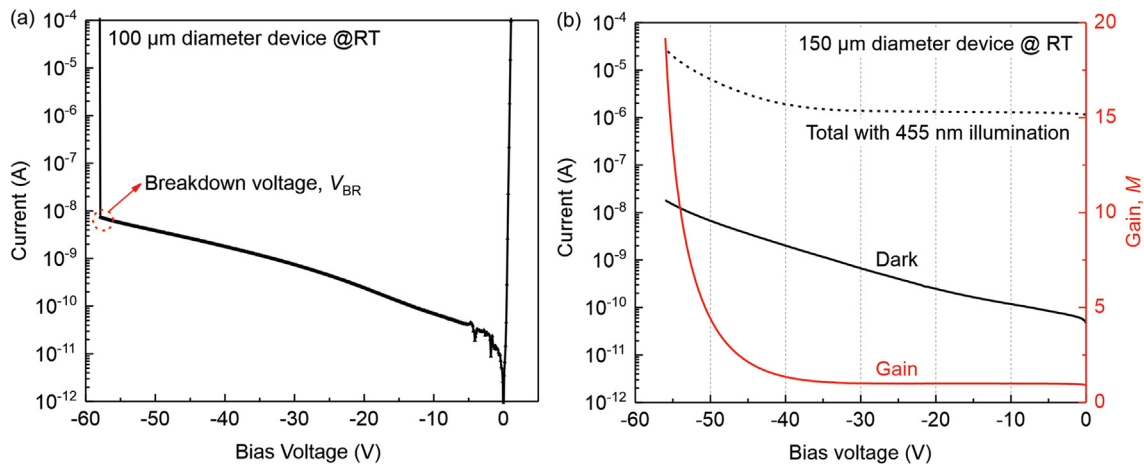


FIG. 5. (a) The measured dark current of the RA AlGaAsSb APD for the 100 μm device at RT. The breakdown occurs at -58 V . (b) The dark current (black solid line), photocurrent (black dashed line), and gain curve (red solid line) of the RA AlGaAsSb APD for the 150 μm device at RT.

orders of magnitude lower than the k of commercial InP (~ 0.5) and AlInAs APDs (~ 0.2), and it is similar to the k of DA AlAsSb (0.005),¹² DA AlGaAsSb (~ 0.01),^{13,32} and RA AlInAsSb (~ 0.014)^{14,33} APDs. Several studies have recently reported reducing the excess noise using the DA method.^{26,34} DA AlInAs particularly shows extremely low excess noise compared with RA AlInAs,³⁴ and it is mainly due to the existence of mini-band in the valence band caused by band structure engineering.³⁴ However, it has also been claimed that using the DA method is not always effective on all material systems.³⁵ For example, InAs/GaAs DA (InGaAs) on InP and AlAs/GaAs DA (AlGaAs) on GaAs did not show an improvement in their excess noise.³⁵ Therefore, it is believed that the AlGaAsSb alloy on InP is a material that does not show a significant difference in the excess noise between the DA and the RA. Possibly, the origin of the low excess noise in the AlGaAsSb alloy is the modified valence band structure, which is caused by incorporating Sb atoms into the AlGaAs alloy. A similar

phenomenon was observed in other material systems, such as AlAsSb³⁶ and GaAsBi.³⁷

A RA AlGaAsSb multiplier thicker than 910 nm will possibly help to achieve a k lower than 0.01. Generally, the high n_{bg} (larger than $1 \times 10^{16}\text{ cm}^{-3}$) restricts the device from being completely depleted due to the gradient of the built-in electric field, resulting in the ambiguity of determining unity gain point and low multiplication gain. The RA AlGaAsSb multiplier reported here showed a very low n_{bg} of $6\text{--}7 \times 10^{14}\text{ cm}^{-3}$, thus enabling its thickness to be larger than 910 nm by ensuring a nearly flat electric field profile applied in the multiplication region.

In conclusion, the RA, 910 nm thick AlGaAsSb APDs, demonstrate low dark current density ($70\text{ }\mu\text{A}/\text{cm}^2$ at a gain of 10) and low k (0.01). There is an opportunity to further improve the RA AlGaAsSb APD's performance by suppressing the surface dark current and increasing the multiplication layer thickness. Nevertheless, the low

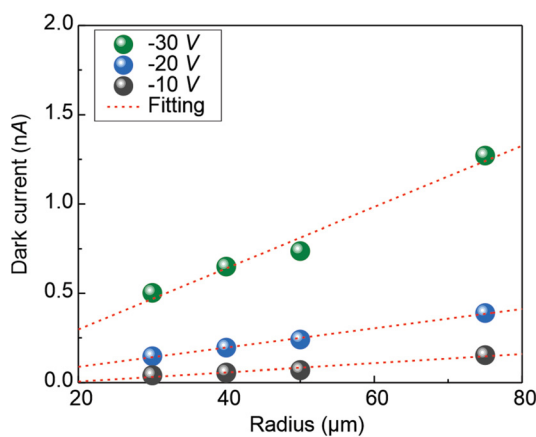


FIG. 6. VADA of the RA AlGaAsSb APD. The measured dark current is plotted with respect to the radius of the devices. The dark current linearly depends on the radius of the devices, indicating that surface dark current dominates the total dark current of the AlGaAsSb APDs.

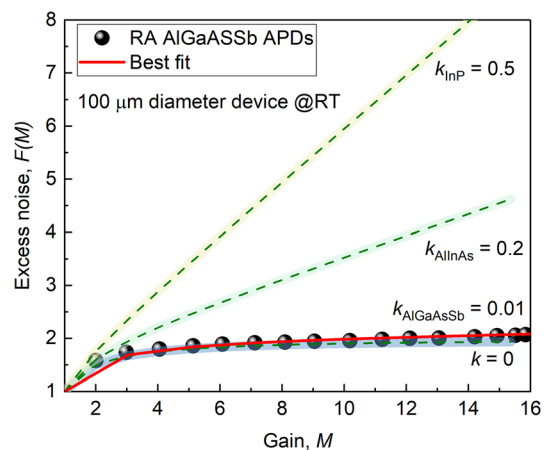


FIG. 7. The measured excess noise, $F(M)$ vs gain, M for the RA AlGaAsSb APD with the 100 μm diameter device. The best fit to the AlGaAsSb APD data found $k=0.01$. The other three $F(M)$ curves correspond to the ideal case of $k=0$ and two commercial multipliers, InP ($k=0.5$) and AlInAs ($k=0.2$).

dark current density, low k , and the anticipated benefit of the RA growth technique suggest that the RA AlGaAsSb APD is a promising multiplier for high-performance and cost-effective APDs. This may also open up a path toward highly sensitive APDs with McIntyre's limit noise characteristics.

This work was supported by the Directed Energy-Joint Technology Office (DE-JTO), Award No. N00014-17-1-2440.

AUTHOR DECLARATIONS

Conflict of Interest

The authors have no conflicts to disclose.

DATA AVAILABILITY

The data that support the findings of this study are available from the corresponding author upon reasonable request.

REFERENCES

- ¹J. C. Campbell, *Optical Fiber Telecommunications VA* (Elsevier, 2008), p. 221.
- ²X. Sun, J. B. Abshire, J. D. Beck, P. Mitra, K. Reiff, and G. Yang, *Opt. Express* **25**, 16589 (2017).
- ³R. J. McIntyre, *IEEE Trans. Electron Devices* **ED-13**, 164 (1966).
- ⁴G. Ribordy, N. Gisin, O. Guinnard, D. Stuck, M. Wegmuller, and H. Zbinden, *J. Mod. Opt.* **51**, 1381 (2004).
- ⁵Voxtel, Inc., see <https://voxtel-llc.com/products/detector-arrays-ingaas-apd/> for "InGaAs APD Detector Arrays."
- ⁶L. W. Cook, G. E. Bulman, and G. E. Stillman, *Appl. Phys. Lett.* **40**, 589 (1982).
- ⁷S. Xie, S. Zhang, and C. H. Tan, *IEEE Photonics Technol. Lett.* **27**, 1745 (2015).
- ⁸M. M. Hayat, B. E. A. Saleh, and M. C. Teich, *IEEE Trans. Electron Devices* **39**, 546 (1992).
- ⁹E. Jamil, J. S. Cheong, J. P. R. David, and M. M. Hayat, *Opt. Express* **24**, 21597 (2016).
- ¹⁰G. J. Rees and J. P. R. David, *J. Phys. D: Appl. Phys.* **43**, 243001 (2010).
- ¹¹X. Yi, S. Xie, B. Liang, L. W. Lim, D. L. Huffaker, C. H. Tan, and J. P. R. David, *Proc. SPIE* **11540**, 115400M (2020).
- ¹²X. Yi, S. Xie, B. Liang, L. W. Lim, J. S. Cheong, M. C. Debnath, D. L. Huffaker, C. H. Tan, and J. P. R. David, *Nat. Photonics* **13**, 683 (2019).
- ¹³S. Lee, S. H. Kodati, B. Guo, A. H. Jones, M. Schwartz, M. Winslow, C. H. Grein, T. J. Ronningen, J. C. Campbell, and S. Krishna, *Appl. Phys. Lett.* **118**, 081106 (2021).
- ¹⁴S. H. Kodati, S. Lee, B. Guo, A. H. Jones, M. Schwartz, M. Winslow, N. A. Pfister, C. H. Grein, T. J. Ronningen, J. C. Campbell, and S. Krishna, *Appl. Phys. Lett.* **118**, 091101 (2021).
- ¹⁵K. Onabe, *Jpn. J. Appl. Phys.* **22**, 287 (1983).
- ¹⁶H. Asahi and Y. Horikoshi, *Molecular Beam Epitaxy: Materials and Applications for Electronics and Optoelectronics* (John Wiley & Sons, 2019).
- ¹⁷S. Tomasulo, M. Gonzalez, M. P. Lumb, C. R. Brown, A. H. Dicarolo, I. R. Sellers, I. Vurgaftman, J. R. Meyer, R. J. Walters, and M. K. Yakes, *J. Cryst. Growth* **548**, 125826 (2020).
- ¹⁸T. Brown, A. Brown, and G. May, *J. Vac. Sci. Technol. B* **20**(4), 1771 (2002).
- ¹⁹M. Losurdo, P. Capezzuto, G. Bruno, A. S. Brown, T. Brown, and G. May, *J. Appl. Phys.* **100**, 013531 (2006).
- ²⁰Y. Hu, M. C. Tam, and Z. R. Wasilewski, *J. Vac. Sci. Technol. B* **37**, 032902 (2019).
- ²¹S. Lee, H. J. Jo, S. Mathews, J. A. Simon, T. J. Ronningen, S. H. Kodati, D. R. Fink, J. S. Kim, M. Winslow, C. H. Grein, A. H. Jones, J. C. Campbell, and S. Krishna, *Appl. Phys. Lett.* **115**, 211601 (2019).
- ²²J. Spitzer, A. Höpner, M. Kuball, M. Cardona, B. Jenichen, H. Neuroth, B. Brar, and H. Kroemer, *J. Appl. Phys.* **77**, 811 (1995).
- ²³T. M. Diallo, A. B. P. Mbeunmi, M. E. Gahouchi, M. Jellite, R. Arvinte, M. R. Aziziyan, R. Arès, S. Fafard, and A. Boucherif, *J. Vac. Sci. Technol. B* **37**, 031208 (2019).
- ²⁴R. Bhat, M. A. Koza, K. Kash, S. J. Allen, W. P. Hong, S. A. Schwarz, G. K. Chang, and P. Lin, *J. Cryst. Growth* **108**, 441 (1991).
- ²⁵S. F. Yoon, Y. B. Miao, and K. Radhakrishnan, *Thin Solid Films* **279**, 11 (1996).
- ²⁶S. Lee, M. Winslow, C. H. Grein, S. H. Kodati, A. H. Jones, D. R. Fink, P. Das, M. M. Hayat, T. J. Ronningen, J. C. Campbell, and S. Krishna, *Sci. Rep.* **10**, 16735 (2020).
- ²⁷X. Zhou, S. Zhang, J. P. R. David, J. S. Ng, and C. H. Tan, *IEEE Photonics Technol. Lett.* **28**, 2495 (2016).
- ²⁸J. Shen, H. Goronkin, J. D. Dow, and S. Y. Ren, *J. Vac. Sci. Technol. B* **13**, 1736 (1995).
- ²⁹J. Shen, H. Goronkin, J. D. Dow, and S. Y. Ren, *J. Appl. Phys.* **77**, 1576 (1995).
- ³⁰J. Li, Z. Xu, P. Han, J. Chen, and X. Ji, *Opt. Express* **26**, 15308 (2018).
- ³¹B. Guo, A. H. Jones, S. Lee, S. H. Kodati, B. Liang, X. Xue, N. A. Pfister, M. Schwartz, M. Winslow, C. H. Grein, T. J. Ronningen, S. Krishna, and J. C. Campbell, *Appl. Phys. Lett.* **119**, 171109 (2021).
- ³²S. Lee, S. H. Kodati, B. Guo, A. H. Jones, M. Schwartz, H. Jung, N. Pfister, M. Winslow, C. H. Grein, T. J. Ronningen, J. C. Campbell, and S. Krishna, *Proc. SPIE* **11741**, 117410B (2021).
- ³³S. H. Kodati, S. Lee, B. Guo, A. H. Jones, M. Schwartz, M. Winslow, N. A. Pfister, C. H. Grein, T. J. Ronningen, J. C. Campbell, and S. Krishna, *Proc. SPIE* **11741**, 117411X (2021).
- ³⁴J. Zheng, Y. Yuan, Y. Tan, Y. Peng, A. K. Rockwell, S. R. Bank, A. W. Ghosh, and J. C. Campbell, *J. Lightwave Technol.* **36**, 3580 (2018).
- ³⁵A. K. Rockwell, M. Ren, M. Woodson, A. H. Jones, S. D. March, Y. Tan, Y. Yuan, Y. Sun, R. Hool, S. J. Maddox, M. L. Lee, A. W. Ghosh, and J. C. Campbell, *Appl. Phys. Lett.* **113**, 102106 (2018).
- ³⁶X. Jin, S. Xie, B. Liang, X. Yi, H. Lewis, L. W. Lim, Y. Liu, B. K. Ng, D. L. Huffaker, C. H. Tan, D. S. Ong, and J. P. R. David, *IEEE J. Sel. Top. Quantum Electron.* **28**, 1 (2022).
- ³⁷Y. Liu, X. Yi, N. J. Bailey, Z. Zhou, T. B. O. Rockett, L. W. Lim, C. H. Tan, R. D. Richards, and J. P. R. David, *Nat. Commun.* **12**, 4784 (2021).